Device Modeling of Superconductor Transition-Edge Sensors Based on the Two-Fluid Theory

Tian-Shun Wang, Guang-Can Guo, Qing-Feng Zhu, Jun-Xian Wang, Tie-Fu Li, Jian-She Liu,
Wei Chen, and Xingxiang Zhou

Abstract—In order to support the design and research of sophisticated large-scale transition-edge sensor (TES) circuits, we use basic SPICE elements to develop device models for TESs based on the superfluid–normal fluid theory. In contrast to previous studies, our device model is not limited to small-signal simulation, and it relies only on device parameters that have clear physical meaning and can be easily measured. We integrate the device models in design kits based on powerful electronic design automation tools such as CADENCE and OrCAD and use them for versatile simulations of TES circuits. Comparing our simulation results with published experimental data, we find good agreement which suggests that device models based on the two-fluid theory can be used to predict the behavior of TES circuits reliably. Hence, they are valuable for assisting the design of sophisticated TES circuits.

Index Terms—Device model, SPICE, superfluid–normal fluid, transition-edge sensor (TES).

I. INTRODUCTION

THE PAST two decades have witnessed the rapid development of the superconductor transition-edge sensor (TES) technology [1] and its successful application in a wide range of scientific and instrumental fields [2]–[6]. Most impressively, mid-scale TES detector arrays with tens to hundreds of pixels have been fabricated and deployed in Astronomy telescopes [7], [8]. In the near future, it is expected that much larger scale TES detector arrays, potentially with thousands to tens of thousands of pixels, will become available [9].

A fully functional TES detector array is a complex superconductor circuit system because all TES sensors at the pixel level need auxiliary supporting circuits for device biasing and signal readout. As the scale of the detector array grows, more system-level circuits such as multiplexers [10]–[12] become indispensable too. It quickly becomes overwhelming to design and integrate all the necessary devices and circuits when the system size becomes large, and this challenge can only be met by elaborate electronic design automation (EDA) tools specifically developed for TES circuits.

Unfortunately, sophisticated tools that can support the simulation and design of large-scale TES circuits are presently unavailable. An important reason for this deficiency is the lack of reliable TES device models that can be integrated in existing EDA tools to predict the behavior of TES circuits accurately. Since TESs are highly nonlinear electrothermal devices, their behavior is complicated, and their modeling is difficult. Most previous research is limited to small-signal models [1] that cannot be used for important tasks such as determining the required dc biases and deriving the temperature sensitivity from easily measurable device parameters. Some studies try to model the temperature dependence of TES resistance using fitting functions such as the hyperbolic function [13], the error function [14], the Fermi function [15], and other expressions [16], [17]. Although convenient in producing resistance–temperature ($R-T$) curves matching experimental data measured under certain conditions that are often very different than the actual working conditions for the TES devices (see Section IV-A), these models are not based on sound physical considerations, and their applicability is difficult to justify. More seriously, since TESs are highly nonlinear devices, their $R-T$ dependence and electrical and thermal behavior are very sensitive to how the circuits are designed and biased, as well as how the system is operated and how the $R-T$ curves are measured (see Section IV-A). The fitting function approach that models the TES resistance as a sole function of the device temperature cannot capture this critical dependence on TES device's working conditions, and hence, it is fundamentally flawed.

With the long-term goal of making highly capable and integrated EDA tools that can support the design and simulation of large-scale TES circuits, in this paper, we develop device models for TESs based on the superfluid–normal fluid theory. We choose SPICE as the modeling tool and use only the most basic SPICE circuit elements in order to be able to integrate our device model in the widest possible variety of circuit simulators. With the two-fluid theory as the underlying physical mechanism, the device model has the advantage that it only relies on device parameters that have clear physical meaning and can be easily measured. After integrating the device models in design kits based on powerful EDA tools such as CADENCE [18] and OrCAD [19], we then use them to perform a variety of simulations of TES circuits and compare the results to

published experimental data to test the validity and accuracy of the device models.

II. DEVICE PHYSICS

In this section, we study the device physics that our TES model is based on. Since the TES sensor is an electrothermal device, we divide our discussion into the electric and thermal properties of the TES device.

A. Electric Behavior

The functioning of a TES sensor relies on the sharp transition between the device's superconducting and normal states, which is a very complex process. There are two well-known theories to describe the transition physics, namely, the Skocpol–Beasley–Tinkham (SBT) model [20] based on the phase-slip events in type-I superconductors and the Kosterlitz–Thouless–Berezinsky (KTB) model [21], [22] based on flux vortex creation and interaction in type-II superconductors. Although all superconductors used to fabricate TES devices are of type I, some authors argue that in 2-D thin films, the vortex model is applicable [23]. There is also experimental evidence that the longitudinal proximity effect may play an important role in the TES physics [24]. The question as to which theory should be used to build electronic models that can describe TES device's behavior accurately, or whether any model will be suitable for this purpose at all, can only be answered by comparing the predicted behavior with experimentally measured data.

In our work, we are interested in building a simple model that captures the most important elements of the device physics and, thus, can be easily used to simulate the behavior of the TES device with reasonably good accuracy. For this purpose, we consider a simplified two-fluid model [25], which has its root in the SBT theory. In this model, the sensor current is separated into a supercurrent I_s and a normal current I_n. The total current is then

$$I = I_s + I_n \tag{1}$$

and a voltage V can appear across the TES device because of the normal current. According to the SBT theory, the supercurrent $I_s = C_I I_c(T)$, where $I_c(T)$ is the temperature-dependent critical current of the TES film, and C_I is the ratio of the time-averaged critical current in the phase slip lines to I_c. The normal current I_n can be associated with the voltage across the device by $I_n = V/(C_n R_n)$, where R_n is the normal state resistance of the TES device, and C_n (usually approximately equal to 1) is the ratio of the total resistance of the phase slip lines in the TES film to R_n.

In the two-fluid theory, the temperature dependence of the device's critical current I_c plays an essential role. In our simplified device model, it is the underlying mechanism for the temperature dependence of the TES resistance. For simple Bardeen-Cooper-Schrieffer (BCS) superconductors that behave in accordance with the Ginzburg–Landau theory, we have

$$I_s = I_{s0}(1 - t)^{3/2} \tag{2}$$

where I_{s0} is the supercurrent of the TES device at 0 temperature, and $t = T/T_c$ is the temperature normalized to the device's critical temperature. For a single-layer uniform film, the critical current can be expressed as a function of the sample's other parameters such as the heat capacity and normal resistance [25]. Since most TES devices consist of multilayer films made of different metals, we do not expect this relation to hold, and the supercurrent I_{s0} is an independent parameter in our device model. Nonetheless, the supercurrent and its temperature dependence can be easily measured.

Summarizing the main elements in the simplified two-fluid model, we can express the TES device's equivalent resistance as

$$R = \frac{V}{I_{s0} \left(1 - \frac{T}{T_c}\right)^{3/2} + V/(C_R R_n)} \tag{3}$$

where V is the voltage across the device. The nonlinear resistance described in (3) is implemented in our device model with the critical temperature T_c, supercurrent I_{s0}, and normal resistance R_n being independent device parameters. Although highly simplified, it focuses on the most important mechanism underlying the TES device, and simulation results based on it are consistent with many qualitative conclusions derived from experimental data (see Section IV). Notice that we have assumed 0 applied magnetic field. In addition, for simplicity, we have used $C_R = 1$ in our device model,[1] although it has been shown that its value can be different than 1 by fitting experimental data [26]. In general, C_R can be a function of temperature and other variables; however, there are no known reliable methods to calculate and measure its temperature dependence. The effect of magnetic fields, the temperature dependence of C_R, as well as other factors that can affect TES device's behavior, will be considered in improved versions of the device model.

B. Thermodynamics

The thermal behavior of the TES device is dictated by the interplay of the Joule heating due to the device current and the heat conduction to the substrate. To describe the involved physics, we use a thermal model as shown in Fig. 1, which consists of an absorber, the TES device, and the substrate. This model includes the thermal complexity that is sufficient to describe most TES devices. Notice that, if we assign a very large value to the absorber-TES heat conduction coefficient K_2, the heat conduction between them is very efficient, and they will remain at the same temperature. Therefore, the thermal model in Fig. 1 applies to devices without a dedicated absorber too.

We assume that heat conduction between the absorber, the TES, and the substrate are governed by the power law, i.e.,

$$P = K \left(T_a^n - T_b^n\right) \tag{4}$$

---

[1]A nonunity but constant C_R only complicates the details of our device model slightly. Although we could easily revise our device model to allow the value of C_R to be specified by the model user, C_R does not satisfy the requirement of being a parameter that has clear physical meaning and can be easily measured.
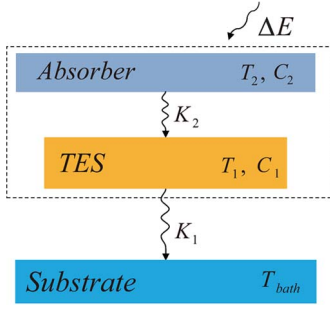
Fig. 1. Heat generation and conduction in the absorber-TES-substrate structure.

where P is the power flow between two elements a and b, T_a and T_b are their temperatures, K is the conduction coefficient, and n is the exponent. Assuming the substrate temperature is fixed at T_{bath}, we can then write the thermal equation for the TES as

$$C_1 \frac{dT_1}{dt} = IV - K_1 \left(T_1^{n_1} - T_{\text{bath}}^{n_1}\right) + K_2 \left(T_2^{n_2} - T_1^{n_2}\right) \quad (5)$$

where T_1 and T_2 are the temperatures of the TES and absorber; C_1 is the heat capacity of the TES; I is the current through the TES; V is the voltage across the TES; and K_1, K_2, n_1, and n_2 characterize the TES-substrate and absorber-TES heat conduction. In (5), the terms on the right-hand side correspond to Joule heating and heat conduction to the substrate and from the absorber. Similar consideration leads to the thermal equation for the absorber, i.e.,

$$C_2 \frac{dT_2}{dt} = P_s - K_2 \left(T_2^{n_2} - T_1^{n_2}\right) \quad (6)$$

where C_2 is the heat capacity of the absorber, and P_s is the signal power.

Equations (5) and (6) are the basis of the thermal part of our device model, which has C_1, C_2, K_1, K_2, n_1, and n_2 as its independent parameters. These device parameters have clear physical meaning. Their values depend on the materials and geometries of the device and can be measured by established experimental techniques. For simplicity, we have neglected the temperature dependence of these device parameters, which should be weak in the temperature ranges that we are interested in.

III. MODELING TECHNIQUES

The two options available for TES device modeling are SPICE and analog hardware description language (HDL). In simulating and debugging TES circuits, we often need to examine signals on the internal nodes of the TES device. Behavior models built with analog HDL are less convenient for this purpose. In addition, these models tend to be less efficient in circuit simulation, and their integration in SPICE and SPICE-like circuit simulators requires some effort. Because of these considerations, we choose SPICE as our modeling tool.

Although we have simplified the device physics as much as possible in Section II, building SPICE models for the

TES device is still quite involved. The main challenge lies in constructing equivalent electric circuit for the thermal part of the device model and modeling the nonlinear elements and processes in the device. Many latest circuit simulators have built-in nonlinear dependent source support. However, the syntax is simulator specific, and the implementation details also vary. In order to be able to integrate our device model in the widest possible variety of circuit simulators, we choose to model the TES device using the polynomial-controlled source, which is supported in almost all circuit simulators.

The polynomial-controlled source [27] is a circuit element between two nodes whose voltage or current is dependent on one or more controlling signals. In the element description, the number of controlled signals, the nodes for the control signals, the polynomial coefficients, and the initial conditions for the controlling signals can be specified. For instance, a voltage-controlled voltage source Exx between the positive node N+ and negative node N− can be described as Exx N + N − POLY(ND)(NC1 + NC1−)...P0P1...IC = ..., where ND is the number of dimensions (i.e., the number of controlling signals), NC1+, NC1 − ... are the positive and negative nodes of the controlling signals, P0, P1... are the polynomial coefficients, and the optional values following IC = specify the initial conditions for the controlling signals. Take as an example a 2-D voltage source with controlling signals V_a and V_b, the controlled voltage V_c is

$$V_c = P_0 + P_1 V_a + P_2 V_b + P_3 V_a^2 + P_4 V_a V_b + P_5 V_b^2 + \dots. \quad (7)$$

Seemingly simplistic, the polynomial-controlled source is extremely powerful and can be used to realize many operations on multiple electric signals [28]. For example, the circuit in Fig. 2(a) realizes the addition between two voltages V_{12} and V_{34} with a polynomial-controlled source

E1 5 6 POLY(2) (1 2) (3 4) 0 1 1.

To realize the multiplication between them, use the polynomial-controlled source

E1 5 6 POLY(2) (1 2) (3 4) 0 0 0 0 1

instead, as shown in Fig. 2(b). For division between two voltages V_{12} and V_{34}, we use the circuit in Fig. 2(c) where the two voltage-controlled current sources

G1 0 10 POLY(1) (1 2) 0 1

and

G2 10 0 POLY(2) (3 4) (10 0) 0 0 0 0 1

play the central role. Since the currents in the two sources are $I_{\text{G1}} = V_{12}$ and $I_{\text{G2}} = V_{34} V_{10}$ in value, we have $V_{10} = (I_{\text{G1}} - I_{\text{G2}})R_{10} = (V_{12} - V_{34}V_{10})R_{10}$. From this, we can solve for the voltage across nodes 10 and 0, which is

$$V_{10} = \frac{V_{12}}{V_{34} + 1/R_{10}} \approx \frac{V_{12}}{V_{34}} \quad (8)$$
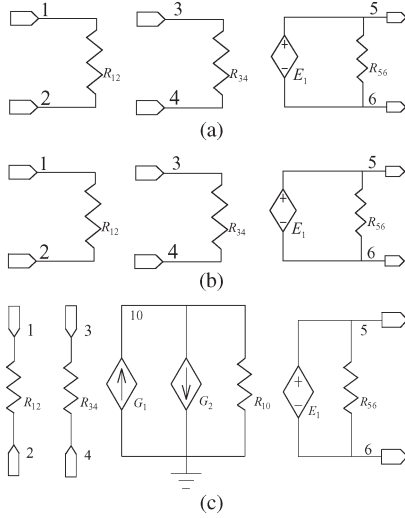
Fig. 2. Polynomial-controlled-source-based circuits to add, multiply, and divide two voltage signals. (a) Adder circuit between two voltages V_{12} and V_{34}. E1 is the polynomial-controlled source. The output signal $V_{56} = V_{12} + V_{34}$. The resistances R_{12}, R_{34}, and R_{56} are chosen very large (e.g., 1G Ω) to ensure that the input and output resistances are large. (b) Multiplier circuit between two voltages V_{12} and V_{34}. The output signal $V_{56} = V_{12}V_{34}$. R_{12}, R_{34}, and R_{56} are chosen to be very large. (c) Divider circuit for V_{12} and V_{34}. All resistances are large. The output signal $V_{56} = V_{12}/V_{34}$.

as long as the resistance R_{10} is large. The voltage-controlled voltage source

$$\texttt{E1 5 6 POLY(1) (10 0) 0 1}$$

in parallel with the large resistance R_{56} simply mirrors the voltage V_{10} so that the output voltage V_{56} is the division between the input voltages V_{12} and V_{34}.

In the following, we explain how the electric and thermal part of the TES physics and the coupling and feedback between them are modeled. We also present relevant circuit diagrams.

A. Electric Behavior Modeling

In order to model the voltage- and temperature-dependent TES resistance in (3), we use the circuits shown in Fig. 3. At the heart of the circuit is the effective voltage-controlled resistance in Fig. 3(a) realized by the following polynomial voltage-controlled current source

$$\texttt{FIN 2 10 POLY(2) VIN VI 0 0 0 0 1.}$$

The current in this controlled current source FIN is

$$I_{\texttt{FIN}} = I_{\texttt{VIN}} I_{\texttt{VI}} \tag{9}$$

where $I_{\texttt{VIN}}$ and $I_{\texttt{VI}}$ are currents in the auxiliary 0 voltage sources VIN and VI. $I_{\texttt{VI}}$ can be calculated from the voltage of the voltage-controlled voltage source

$$\texttt{E1 20 0 POLY(1) (3 4)} -1\ 1$$

and its value is (R1 = 1 Ω)

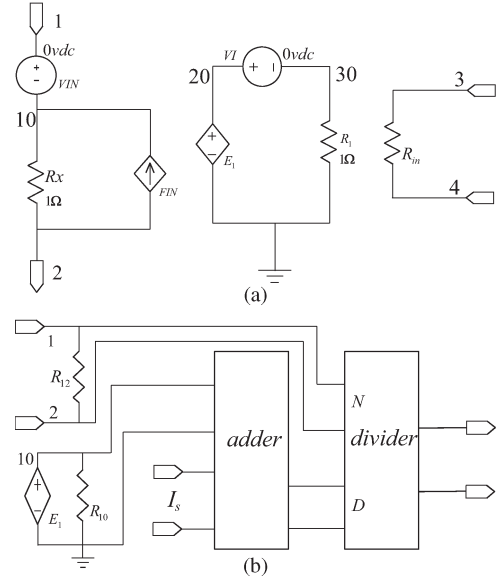$$I_{\texttt{VI}} = V_{\texttt{E1}}/\texttt{R1} = V_{34} - 1 \tag{10}$$

Fig. 3. Circuit model for the TES resistance. (a) Voltage-controlled resistance between nodes 1 and 2. R_x and R_1 are 1 Ω. The input resistance R_{in} is large. (b) Circuit to supply the input control voltage to the voltage-controlled resistance circuit in (a). R_{12} and R_{10} are large. V_{12} is the voltage across the TES device. The adder circuit is that in Fig. 2(a). The divider circuit (N and D refer to terminals for the numerator and denominator signals) is shown in Fig. 2(c). The input signal I_s is a voltage with a value equal to the supercurrent of the TES. It is supplied by the circuit in Fig. 5(a).

where V_{34} is the voltage across nodes 3 and 4. Since the total current through the resistor Rx is

$$I_{\texttt{Rx}} = I_{\texttt{VIN}} + I_{\texttt{FIN}} = I_{\texttt{VIN}} V_{34} \tag{11}$$

the voltage across nodes 1 and 2 is $V_{12} = R_x I_{\texttt{Rx}} = I_{\texttt{VIN}} R_x V_{34}$. The effective resistance between nodes 1 and 2 can then be calculated to be $(R_x = 1\ \Omega)$

$$R_{12} = \frac{V_{12}}{I_{\texttt{VIN}}} = V_{34}. \tag{12}$$

Notice that the effective resistance across terminals 1 and 2 is controlled by the voltage V_{34}. If we design the circuit appropriately so that V_{34} is related to the voltage across nodes 1 and 2 by the expression on the right-hand side of (3), we can then effectively realize a TES resistance across these two nodes. This can be done by using the circuit in Fig. 3(b). This circuit has two inputs, i.e., the TES voltage V_{12} and another voltage equal to the TES supercurrent I_s in value. The TES voltage is scaled by the voltage-controlled voltage source

$$\texttt{E1 10 0 POLY(1) (1 2) 0 1}/R_n$$

and fed into the adder circuit that has I_s as its other input. The input signals to the divider circuit are the TES voltage and the output from the adder circuit. The effective resistance across nodes 1 and 2 in Fig. 3(a) is then

$$R_{12} = \frac{V_{12}}{I_s + \frac{V_{12}}{R_n}} \tag{13}$$

where I_s is the supercurrent, and R_n is the normal resistance of the TES device. The two-fluid-theory-based electric behavior of the TES device is then successfully modeled by our circuit.

B. Thermodynamics Modeling

SPICE is not designed to simulate thermodynamics. Although users can specify a temperature in circuit simulation, it is a constant ambient temperature used by device models to determine the electric characteristics of circuit elements (e.g., the diode current depends on not only its voltage bias but also the operation temperature). In order to study how the temperature of the TES device depends on its working condition, as well as how it changes in time, we must build an equivalent electric circuit to simulate its thermodynamics.

As shown in Fig. 4(a), the thermal equation (5) for the TES film can be mapped to the electric equation of a capacitor being charged by current sources whose values are given by the terms on the right-hand side of the equation. The voltage across the capacitor corresponds to the temperature of the TES device, and the value of the capacitance is the heat capacity of the device. The current terms are dependent on the electric signals and temperature of the TES; thus, they can be modeled by controlled polynomial sources.

The circuit to model the Joule heating in (5) is shown in Fig. 4(b). In this circuit, the voltage-controlled voltage source

    E1 20 0 POLY(1) (10 2) 0 1

simply duplicates the voltage V_{Rx} across the resistor Rx so that $V_{\text{E1}} = V_{\text{Rx}}$. The resistor R1 = 1 Ω converts V_{E1} to a current I_{V1} that is equal to V_{Rx} in value, i.e.,

$$I_{\text{V1}} = V_{\text{E1}}/\text{R1} = V_{\text{Rx}}. \tag{14}$$

Current in the current-controlled polynomial current source

    F1 3 4 POLY(2) V0 V1 0 0 0 0 1

is then

$$I_{\text{F1}} = I_{\text{V0}} I_{\text{V1}} = I_{\text{Rx}} V_{\text{Rx}} \tag{15}$$

which is equal to the Joule heat in the resistor Rx. Using the TES device in place of Rx, we can then wire the controlled current source F1 in Fig. 4(a) for I_{P_J} to model the Joule heat dissipated by the TES device.

The heat conduction terms on the right-hand side of (5) can be directly modeled by controlled polynomial sources. In Fig. 4(c), the voltage-controlled polynomial voltage sources

    E1 10 0 POLY(1) (1 2) 0 0 0 0 0 1

and

    E1 20 0 POLY(1) (3 4) 0 0 0 0 0 1

produce two voltages $V_{10} = V_{12}^5$ and $V_{20} = V_{34}^5$, where V_{12} and V_{34} represent temperatures of structures in the TES. The
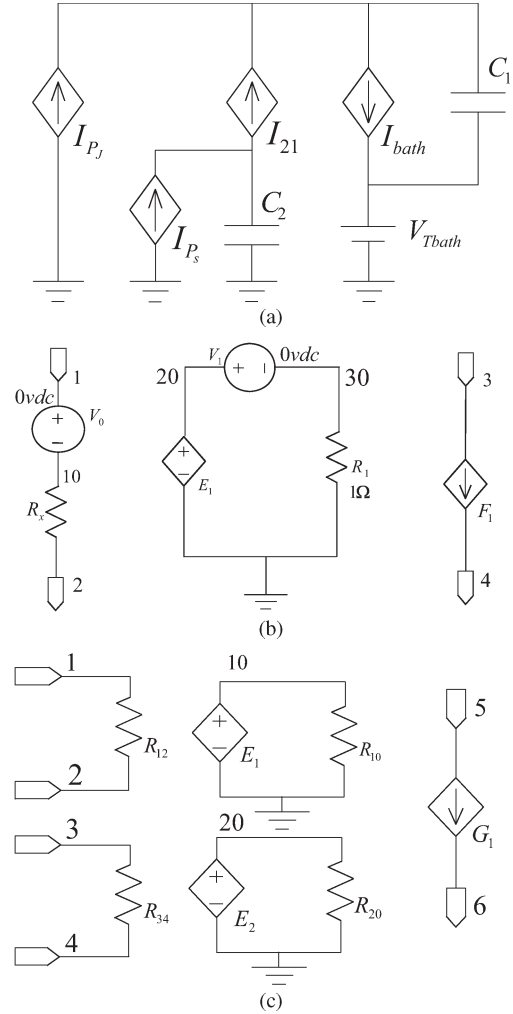

Fig. 4. Equivalent electric circuit for the thermal process in the TES film. (a) Equivalent electric circuit for the thermodynamics of the TES. C_1 and C_2 are the heat capacities of the TES and absorber. The voltage $V_{T\text{bath}}$ represents the environment temperature. Voltages on C_1 and C_2 represent the TES and absorber temperatures. I_{P_J} and I_{P_S} are the Joule heat of the TES and the signal power. I_{bath} and I_{21} are the heat conduction to the substrate and from the absorber. (b) Circuit to model the Joule heat in resistor R_x. The resistance $R_1 = 1$ Ω. (c) Circuit to model the heat flow in the TES that obeys the power law. R_{12}, R_{34}, R_{10}, and R_{20} are large.

polynomial-controlled current source

    G1 5 6 POLY(2) (10 0) (20 0) 0 K − K

then realizes a heat flow of $K(V_{12}^5 - V_{34}^5)$. The heat conduction exponents n_1 and n_2 in (5) are material dependent, and a value of 4 or 5 is often used. If n happens to be a noninteger (but rational) number, it can be written as a fraction. From the numerator and denominator of the fraction, we can construct appropriate power and root circuits using polynomial-controlled sources and realize the corresponding heat flow.

Once we have mapped the temperature of the TES to the voltage of a capacitor and modeled the Joule heat of the TES and its heat flow to other parts of the system using polynomial-controlled sources, we can then use the circuit in Fig. 4(a) to describe the thermal processes in the TES. The thermodynamics of the absorber in (6) can be modeled using the same techniques.
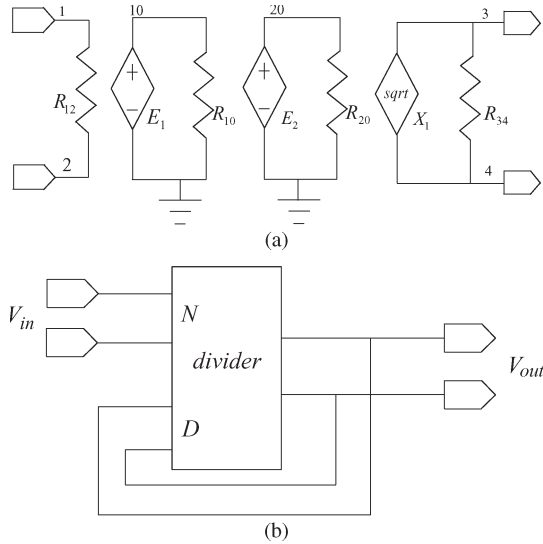
Fig. 5. Circuit to model the temperature dependence of the supercurrent. (a) Circuit to model the temperature-dependent supercurrent of the TES. R_{12}, R_{10}, R_{20}, and R_{34} are large. (b) Square root circuit. The divider circuit is shown in Fig. 2(c).

C. Electrothermal Coupling and Feedback

The key to the operation of the TES device is the negative electrothermal feedback. When the temperature of the TES rises due to the absorption of signal power, the resistance of the device changes. This has the effect of changing the current and Joule power of the device and its heat flow to the substrate, which, in turn, regulates the temperature of the device.

The effect of the TES resistance on the Joule power is already modeled in the thermal circuit in Fig. 4(b) where the equivalent current source for the Joule heat is realized by a polynomial current source controlled by the voltage and current of the TES. When the nonlinear resistance of the TES device changes, so does its Joule power.

The effect of the TES temperature on the device's electric behavior is manifested in the TES resistance in (3) where the supercurrent changes with temperature. In order to model this dependence, we use the circuit in Fig. 5(a). In this circuit, the input voltage V_{12} corresponds to the device temperature T, and the voltage-controlled voltage sources

$$E1 \ 10 \ 0 \ \text{POLY(1)} \ (1 \ 2) \ 1 \ - 1/T_c$$

$$E2 \ 20 \ 0 \ \text{POLY(1)} \ (10 \ 0) \ 0 \ 0 \ 0 \ I_{s0}^2$$

in combination with the square root circuit

$$X1 \ 20 \ 0 \ 3 \ 4 \ \text{sqrt}$$

produce an output signal

$$I_{s0} \left(1 - \frac{T}{T_c}\right)^{3/2}. \tag{16}$$

This is the temperature-dependent supercurrent I_s of the TES device, and it is fed into the circuit in Fig. 3(b) to model the TES resistance. The square root circuit is based on the divider circuit as shown in Fig. 5(b), where one of the input voltages to

the divider circuit is set to the output. Since $V_{\text{out}} = V_{\text{in}}/V_{\text{out}}$, we have $V_{\text{out}} = \sqrt{V_{\text{in}}}$.

Once we have designed circuits to model the electric and thermal behavior and the electrothermal feedback, we can construct a complete device model for the TES based on them. Notice that our TES device model is general purpose and can be used for important studies not supported by the small-signal models developed in previous work.

IV. SIMULATION BASED ON THE DEVICE MODEL

Now that we have built the TES device model, we are interested in using it for simulation of TES circuits to test its validity. Considering the simplicity of the model and the large number of poorly understood and controlled factors in TES device fabrication, it is unrealistic to expect that simulation results based on our model will numerically agree with experimental data to exceedingly high precision for every fabricated TES device. However, a correct device model should give results that are consistent with important qualitative conclusions drawn from experimental data. By doing circuit simulation, we can also perform critical research on TES circuit design and operation. This includes important studies not possible before when only small-signal models were available, such as determining the optimal bath temperature and electrical bias points for TES circuit operation and finding the allowed parameter space for TES device fabrication.

For the purpose of circuit simulation, we integrate the device model in popular EDA tools and leverage the power of these tools to carry out our studies. We use CADENCE and OrCAD, which are based on UNIX and WINDOWS platforms, respectively. The integration process mainly involves constructing subcircuits used in the device model, creating symbol views for them, and building a component library that contains the necessary subcircuits and the TES device model circuit itself. Once all subcircuits and components are created and tested, we can then use the graphic user interface provided by the EDA tools to draw TES circuits, specify device parameters, and run simulations. TES devices can be dragged into a circuit schematic and wired up to the rest of the circuit just like any other circuit elements, and the EDA tools will automatically generate the circuit netlists, add the stimulus and device models, and run the simulation using a simulator specified by the user. This greatly improves the efficiency of our research and reduces human error.

In the following, we describe some interesting TES circuit simulations we performed. We also analyze the results and compare them with published experimental data when possible.

A. R−T Dependence

The width of the superconducting-to-normal transition is an important characteristic of the TES because the sharpness of the transition determines its temperature sensitivity. Some authors have tried to model the TES resistance R using fitting functions that give the measured transition width ΔT and normal state
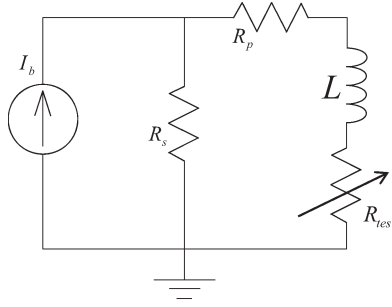
Fig. 6. Voltage-biased TES device. R_s is a small shunt resistance, R_p is the parasitic resistance in series with the TES device, and I_b is the bias current.

resistance R_n. Examples include the hyperbolic function (with the empirical parameter b) [13], i.e.,

$$R(T) = \frac{R_n}{2} \left\{ \tanh \left(\frac{T - T_c}{\Delta T/b} \right) + 1 \right\} \tag{17}$$

the error function [14]

$$R(T) = \frac{R_n}{2} \left\{ \mathrm{erf} \left(\frac{T - T_c}{2\Delta T} \right) + 1 \right\} \tag{18}$$

as well as other mathematical expressions [15]–[17]. One notable problem with the fitting function approach is that the temperature sensitivity calculated from the derivative of the measured $R-T$ curve is often much larger than that inferred from the device's temporal response to a signal pulse. This is because the fitting function approach completely ignores the dependence of the $R-T$ curve on the device's working conditions, which is often critical; we can study this issue using our device model.

The circuit for a voltage-biased TES device is shown in Fig. 6. The $R-T$ curves are usually measured by biasing the TES sample with a constant near 0 current and sweeping the sample temperature. The reason to use a very small bias current is to minimize the Joule heat so that the TES sample remains at the same temperature with the substrate and environment. This temperature can be set and changed by the temperature controller of the refrigerator system, thus making it possible to measure the sample resistance at different temperatures. Not limited to small-signal simulation, our device model applies even in the crossover regime where the TES resistance is not much larger than the shunt resistance. We can use it to simulate this measurement process by a dc analysis in which the environment temperature T_{bath} is the sweeping parameter. For this simulation, we need an exhaustive set of TES device parameters that are, unfortunately, not given in most published works. We use the data from [16], which is relatively complete. The result of the simulation is shown in Fig. 7(a). In order to check that the TES sample remains at the same temperature with the environment, the TES temperature is plotted against the environment temperature in Fig. 7(b). As shown in the figures, although in the transition region the current biases are small enough to produce negligible Joule heat so that the TES sample remains at the same temperature with the environment, the transition width under each bias current can
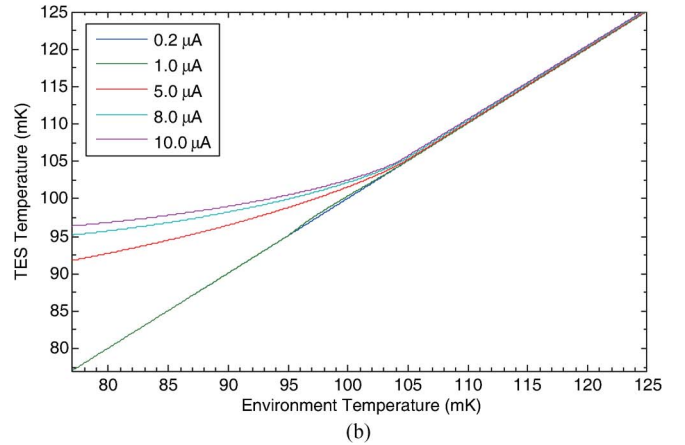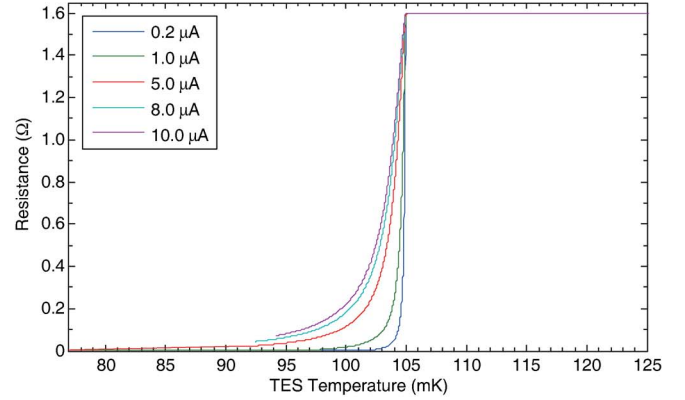

Fig. 7. Simulation of the $R-T$ curve for TES under different bias currents. The device parameters are taken from [16]. The critical temperature of the TES is $T_c = 105$ mK. The TES heat capacity $C = 3.3$ fJ/K. The shunt resistance $R_s = 9.5$ mΩ. The normal state resistance $R_n = 1.6$ Ω. The heat conduction coefficient $K = 16.5$ nW/K^5. The 0 temperature supercurrent I_{s0} is estimated to be 35 μA [see Fig. 10(b)]. (a) Simulated $R-T$ curve for different bias current of the TES device. (b) The TES sample temperature curve.

be quite different. Generally speaking, the smaller the bias current, the sharper the transition. This result clearly indicates that it is fundamentally flawed to model the TES resistance using fitting functions such as those in (17) and (18) without specifying the bias current under which the $R-T$ curve is measured.

The working condition of the TES device is different than that for the $R-T$ curve measurement. The environment temperature is set below the device's critical temperature, and a nonzero bias current is applied to bring the device's temperature to within the transition region. To determine the device's $R-T$ dependence under this working condition, we perform a dc analysis in which T_{bath} is fixed and the circuit's bias current I_b in Fig. 6 is swept. The TES resistance is plotted against the device temperature in Fig. 8.

Comparing the results in Figs. 7 and 8, we notice that the transition width of a working TES device is much wider than that measured with near 0 bias current. While the transition width measured with near 0 current can be as low as sub-millikelvin, the value for a working TES device is a few millikelvins. The transition width can give us an idea of how sensitive the device is to temperature changes under
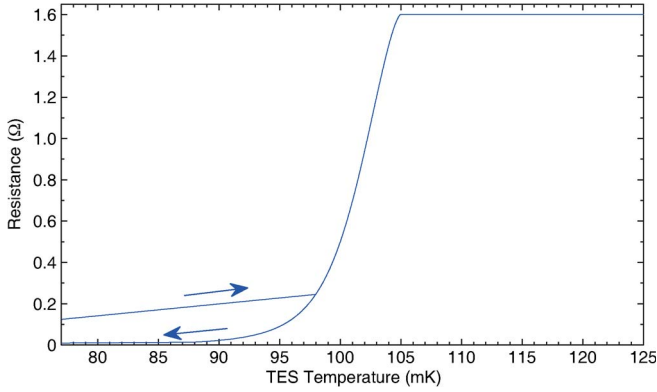
Fig. 8. The resistance–temperature curve of the TES in Fig. 6 produced by sweeping the bias current I_b. The environment temperature is fixed at $T_{\text{bath}} = 55$ mK. The device parameters are the same as those in Fig. 7. Notice that when I_b is swept, there can be gaps in the TES temperature because it can make sharp transitions between the substrate temperature and values close to the critical temperature [see Fig. 9(a)]. This fact is manifested in the straight lines in the figure, which indicate the lack of values (between their end points). Arrows are used to indicate whether the jumps in TES temperature occur when the temperature is increased or decreased.

corresponding working conditions. In small-signal analysis, the temperature sensitivity of the TES is defined by

$$\alpha = \frac{T}{R} \frac{\partial R}{\partial T} \qquad (19)$$

evaluated at fixed TES current (T is the operation temperature of the TES and R the resistance at T). Although the derivative in (19) is not taken along the R–T curve in Fig. 8, we can use its slope for a rough estimate of α. The wide transition width in Fig. 8 then explains why the TES device's temperature sensitivity calculated from the derivative of the measured R–T curve is usually much greater than that inferred from the device's transient response to an input signal. Notice that the R–T dependence in Fig. 8 cannot be easily measured experimentally since the temperature of a working TES device cannot be directly measured. Nevertheless, we can now study it in detail by simulations based on our device model. The benefit of such simulations goes much further. For instance, in setting the working condition for the TES device, it is nontrivial to determine values for the substrate temperature and bias current to optimize the device's temperature sensitivity and other critical characteristics. Circuit simulations can greatly help in finding appropriate bias points and working conditions for the TES device. Otherwise, large number of measurements of the circuit's IV characteristics must be performed.

B. Hysteresis in the Temperature–Bias Current Curve

Another interesting phenomenon of the TES device is that it can display hysteresis when its temperature is adjusted with a bias current. In Fig. 6, when the bias current is increased, the temperature of the TES devices rises above the substrate temperature (i.e., the environment temperature) because of the Joule heating of the TES. Although the temperature–bias current curve cannot be directly measured (due to the difficulty in measuring the temperature of the TES), the characteristics of this curve have profound impact on the operation of the
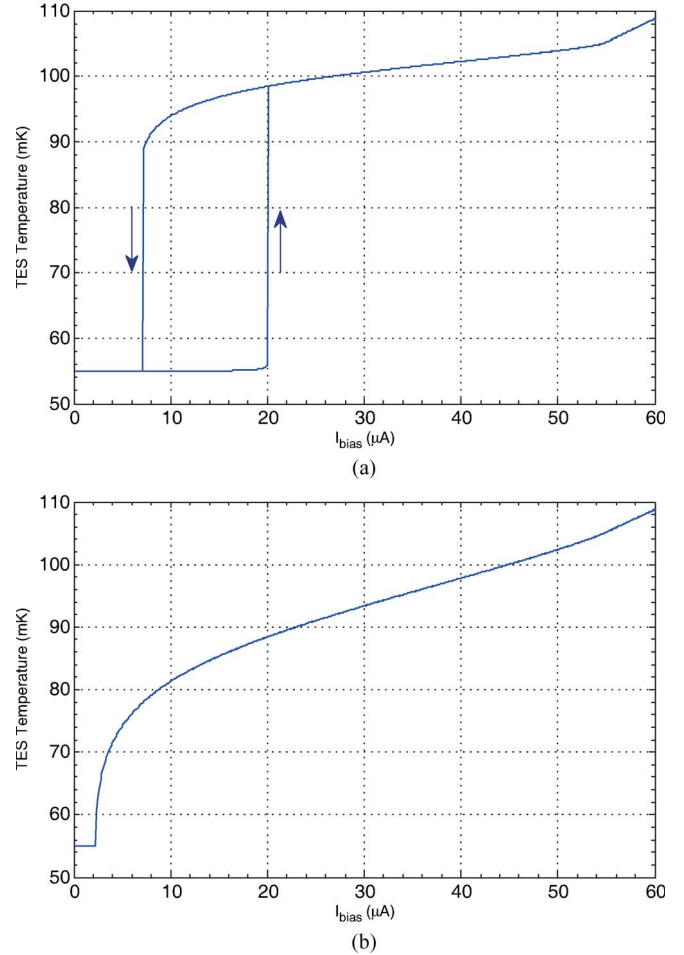

(a)

(b)

Fig. 9. Simulated temperature–bias current curve for the TES for different device parameters. (a) Hysteretic temperature–bias current curve for the TES device. The parasitic resistance is $R_p = 8$ mΩ [see Fig. 10(b)]. The 0 temperature supercurrent $I_{s0} = 35$ μA. The environment temperature is 55 mK. Other device parameters are the same as those in Fig. 7. In order to obtain the hysteretic curve, we use a special bias circuit to control the bias current I_b for the TES circuit in Fig. 6. When the sweeping current in the dc analysis is changed from the minimum to the maximum value, I_b in Fig. 6 changes from 0 to some maximum value and then back to 0. (b) Nonhysteretic temperature–bias current curve. $I_{s0} = 3.9$ μA; other parameters are the same as in (a).

TES device and are, therefore, worth careful investigation. A dc analysis based on our device model can be used for this study.

In Fig. 9, the simulated temperature–bias current curve of voltage-biased TES device with different parameters are plotted. It is shown that when the bias current is increased, the temperature of the TES does not increase with the bias current linearly. Instead, at some bias point, it makes a sharp transition from a value close to the substrate temperature to a value close to the critical temperature of the device. More interestingly, for many device parameters, this sudden transition between near substrate temperature and near critical temperature can exhibit a hysteresis. After the TES temperature has made a sudden transition to close to the critical temperature at some bias current I_{b1}, if we subsequently decrease the bias current, we can bring the device temperature back to close to the substrate temperature. This later temperature transition occurs suddenly too at some bias current I_{b2}, and I_{b2} can be different than I_{b1} giving rise to the hysteresis shown in Fig. 9(a).
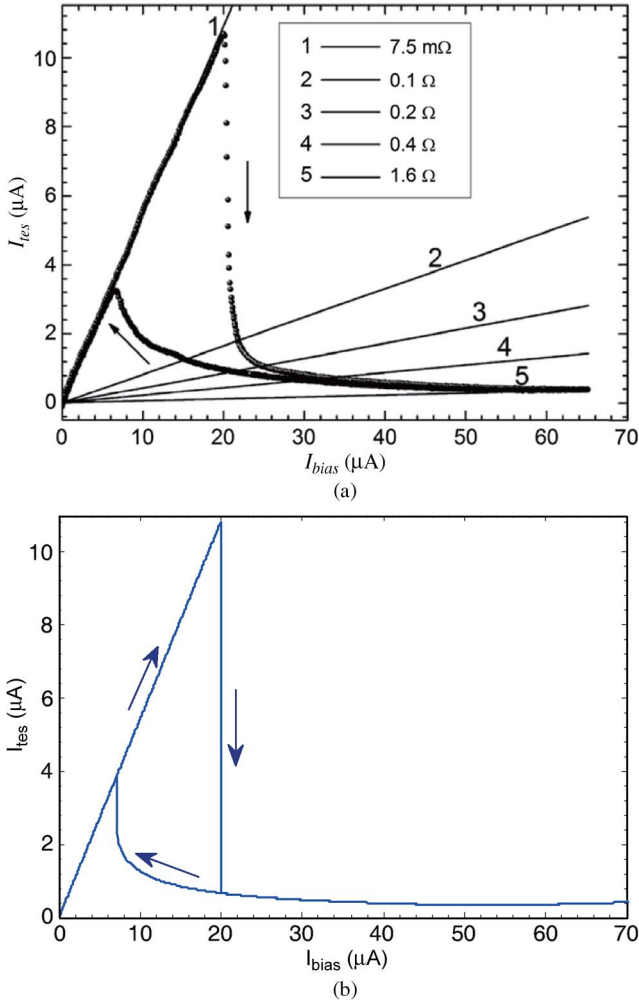
(a)

(b)

Fig. 10. Measured and simulated TES current against total bias current for voltage-biased TES device. (a) Experimentally measured current in the TES against the total bias current in Fig. 6. The curve is taken from [16]. (b) Simulated $I_{tes} - I_{bias}$ curve. Device parameters given in [16] are used (see Figs. 7 and 8). The parasitic resistance for the TES is estimated to be 8 mΩ according to the slope of the superconducting branch in (a) and the value of the shunt resistance R_s. I_{s0} is estimated to be 35 μA. It can be deduced from the BCS temperature dependence for the supercurrent I_s, the fact that the device's temperature jumps from the substrate temperature to a value close to the critical temperature during the superconducting phase transition [see Fig. 9(a)] and the value of the supercurrent when the phase transition occurs [see Fig. 10(a)].

The hysteresis in Fig. 9(a) is a consequence of the nonlinear nature of the TES device. Simulations show that, for certain device parameter ranges, the sudden temperature transition points can be very close to the critical temperature of the device, and this can disrupt the normal operation of the TES and reduce its saturation input energy. In order to avoid such a scenario, care must be taken in the design phase to choose the device parameters correctly before it is fabricated. Such design work relies on large number of simulations of the circuit behavior, and appropriate TES device models are indispensable.

Although the temperature–bias current curve cannot be directly measured to observe the hysteresis in the device temperature, indirect experimental evidence is available. Some authors have measured the current in the TES branch against the total bias current in Fig. 6. The data can consist of a superconducting branch and a resistive branch, as shown in Fig. 10(a). When
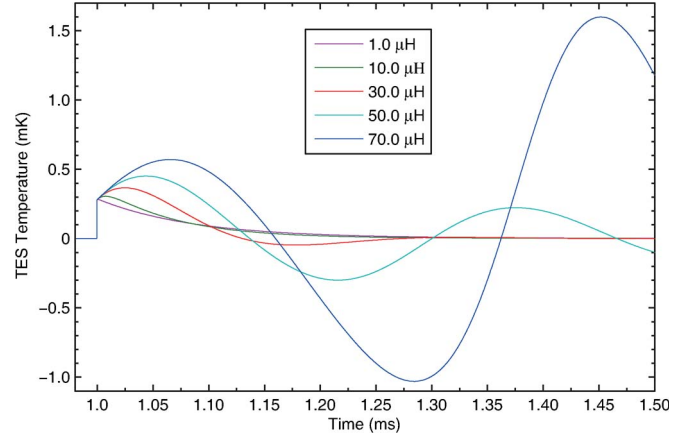

Fig. 11. Parametric simulation of the temporal response of the TES circuit in Fig. 6. The input signal is a short pulse. The temperature change of the TES is plotted as a function of time, for different inductance values. Bias current of the circuit is 30 μA. All other parameters and biases are the same as in previous simulations (see Figs. 7, 8, and 10).

the bias current is decreased from the resistive branch, the TES eventually returns to the superconducting state; however, the bias current at the transition point is different than that for the superconducting to resistive transition, which leads to a hysteresis structure in Fig. 10(a). This is a manifestation of the hysteresis in the TES resistance, which, in turn, is due to the temperature hysteresis in Fig. 9(a). The current curve in Fig. 10(a) can be simulated using our device model, and the result is plotted in Fig. 10(b). The result agrees well with experimental data indicating the effectiveness of the device model.

C. Transient Response to Signal Pulses

Our device model can be directly used in transient and ac analysis to simulate temporal and frequency responses of the TES circuits to input signals. The simulator will automatically linearize the circuit when necessary (e.g., in performing ac analysis), saving the trouble of manually deriving small-signal models.

As an example, we simulate the transient response of the TES circuit in Fig. 6 to an input signal pulse under different circuit parameters. The TES temperature change as a function of time is plotted in Fig. 11. Using the EDA tool's parametric analysis functions, we can perform the same simulation for a range of circuit parameters in just one run and plot the results in the same figure. This makes it convenient to compare the results and observe how the response of the circuit changes with circuit parameters. In Fig. 11, we see that the circuit response becomes unstable when the inductance L increases. This simple parametric simulation then allows us to determine the range of acceptable values of the inductance to ensure the stability of the response (when other circuit parameters are fixed). Although the circuit stability requirement for the inductance is reasonably well described by the small-signal model (if the temperature sensitivity is known) [1], using our device model and similar simulation techniques, we can study how the circuit behavior changes with any device and circuit parameter. This allows us to achieve desirable characteristics for the TES circuit (e.g.,
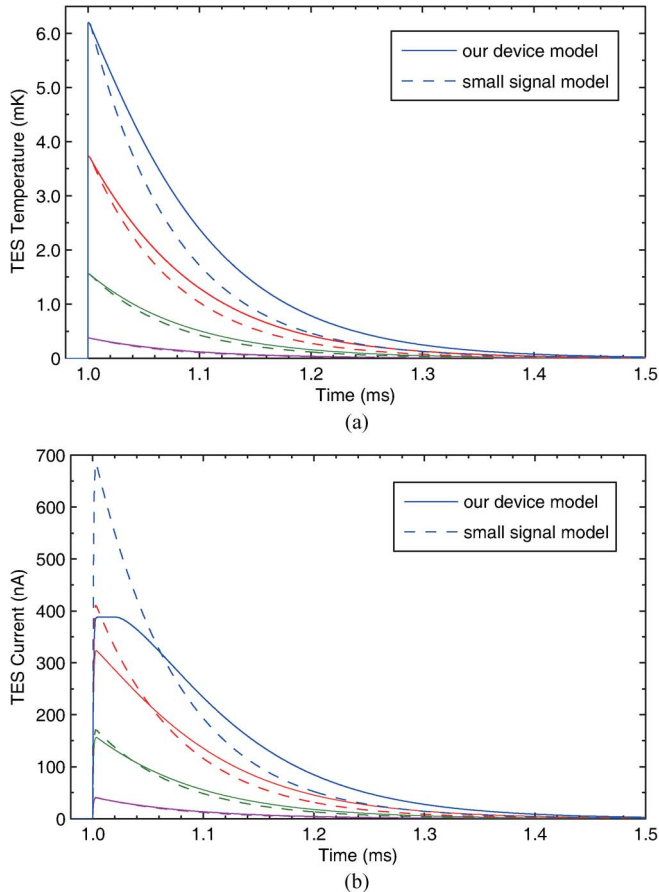
Fig. 12. Comparison between transient simulation results based on our device model and small-signal model for input pulse signals of different energies in Fig. 6. Simulation results corresponding to the same input signal energy are plotted in the same color. Simulation results based on our device model and small-signal model are differentiated by different line styles. The inductance $L = 1 \mu H$. All other parameters are the same as in Fig. 11. (a) TES temperature changes as a function of time. (b) TES current change as a function of time.

by maximizing the temperature sensitivity or optimizing the frequency response), and it is beyond the capabilities of small-signal models. Such search for appropriate circuit parameter values is an important task in circuit design and optimization, and it is much more challenging when multiple parameters need to be simultaneously considered. By developing sophisticated software that intelligently uses parametric simulations based on our device model in a multidimensional parameter space, it is possible to automate the critical task of optimizing circuit parameters [29, 30].

In order to see how simulation results based on our device model compare to those with small-signal models, we perform transient simulations with input pulse signals of different energies using our device model and small-signal model, respectively. The results are plotted in Fig. 12. For the small-signal model simulation, we need the device's temperature sensitivity α and current sensitivity β [1]. Assuming the two-fluid model applies, we perform a dc analysis with our device model to determine the steady state of the system in the absence of signal power. We then calculate α and β at this steady state according to the expression for the TES resistance in (3) [26]. α and β obtained in this manner are used in small-signal model simulations for all input signal energies.

As shown in Fig. 12(a), the simulation results for the TES temperature with our device model and small-signal model are almost identical when the input signal energy is small. However, when the input signal energy becomes large, although the decay time from the small-signal model simulation does not change, simulation results based on our device model start to deviate from those from small-signal model simulations. This trend is even more appreciable in the TES current plot in Fig. 12(b), where the peak heights of the TES current changes are substantially different in simulations based on our device model and small-signal model when the input signal energy is large. Most interestingly, when the signal energy is so large that the TES temperature shoots above the critical temperature [the top-most curves in Fig. 12(a) and 12(b)], the TES current in simulations based on our device model becomes capped. This is because once the TES device becomes normal, its resistance is fixed at R_n, and the TES current is determined by the ratio between R_n and the shunt resistance.

The comparison between simulation results based on our device model and small-signal model indicates that our device model might enable more accurate simulations in situations in which the signals are not necessarily small (such as finding the slew rate of the device). However, we should emphasize that this is not the most important benefit that our model offers. With a clear underlying physical mechanism, our device model allows us to simulate and observe how the behavior of TES circuits is related to the device parameters and other relevant factors (such as bias conditions) and, thus, gain deep understanding of the operation of TES circuits. Knowledge and insights obtained in such studies are very valuable because they can directly guide the design and optimization of TES circuits even if the simulation results are not completely accurate numerically.

A direct comparison of the simulation results in Figs. 11 and 12 to experimental data is hindered by the incompleteness of the device parameters and experimental plots in [16]. However, the device's temperature sensitivity suggested by the simulation appears to be smaller than the values given in the original reference for the same bias current. This indicates that our TES model based on idealized device physics might not give completely accurate numerical results for all TES devices considering the many uncertain and poorly controlled factors in the fabrication process that can impact the characteristics of the fabricated device. A possible reason for the disagreement can be our setting $C_R = 1$ in the device model without considering the possibility of C_R being nonunity [26] or even temperature dependent. It is also conjecturable that the exponent λ in the supercurrent–temperature relation $I_s(T) = I_{s0}(1 - T/T_c)^\lambda$ can deviate from the BCS result $\lambda = 1.5$ in the transition regime for practical devices. It is up to further theoretical and experimental studies to determine whether careful consideration of these issues can explain the discrepancy between the simulation and experimental data and lead to more accurate device models.

Although the example simulations we described in this paper are all based on the simple voltage-biased TES circuit in Fig. 6, more sophisticated circuits can be simulated, and more complex analysis can be performed using our

device model. When the scale of TES sensor array increases, the main challenge will shift from optimization of individual sensor units to design and verification of system-level circuits and architecture. These system-level considerations may include circuits for signal conversion and processing, and they can contain Josephson devices. There is also the possibility of incorporating other advanced superconducting circuit technologies [31]. If we integrate our device model in a circuit simulator like WRspice [32] which supports Josephson devices http://www.wrcad.com/wrspice.html, we will be able to simulate complete superconducting circuit systems that contain both TES devices and supporting Josephson circuits (e.g., SQUID amplifiers, multiplexers, and RSFQ circuits). Such powerful tools will make it possible to design and study large-scale TES circuit systems for future scientific applications.

V. CONCLUSION

In summary, we have developed a simple TES device model based on the superfluid–normal fluid theory. The device model is not limited to small-signal simulations and can be used to study important characteristics of TES circuits and assist their design. Simulation results based on our device model are consistent with important observations and conclusions derived from experimental data, and they can be used to study phenomena not directly measurable in experiments. The device model can be improved by refining the device physics and considering neglected factors. The ideas and techniques used in our work can be also applied to the modeling of other superconductor electrothermal devices such as hot-electron-bolometers [33], [34]. It is hoped that future improved device models will give better accuracy and reliability so that they can be used to develop sophisticated EDA tools that can eventually support the design and simulation of large-scale TES circuits.

REFERENCES

[1] K. D. Irwin and G. C. Hilton, "Transition-edge sensors," *Topics Appl. Phys*, vol. 99, pp. 63–152, 2005.

[2] K. Irwin, G. Hilton, D. Wollman, and J. Martinis, "X-ray detection using a superconducting transition-edge sensor microcalorimeter with electrothermal feedback," *Appl. Phys. Lett*, vol. 69, no. 13, pp. 1945–1947, Sep. 1996.

[3] D. A. Wollman, S. W. Nam, D. E. Newbury, G. C. Hilton, K. D. Irwin, N. F. Bergren, S. Deiker, D. A. Rudman, and J. M. Martinis, "Superconducting transition-edge-microcalorimeter X-ray spectrometer with 2eV energy resolution at 1.5 keV," *Nucl. Instrum. Methods Phys. Res. A, Accel. Spectrom. Detect. Assoc. Equip.*, vol. 444, no. 1/2, pp. 145–150, 2000.

[4] B. Cabrera, R. Clarke, A. Miller, S. W. Nam, R. Romani, T. Saab, and B. Young, "Cryogenic detectors based on superconducting transition-edge sensors for time-energy-resolved single-photon counters and for dark matter searches," *Phys. B*, vol. 280, no. 1–4, pp. 509–514, 2000.

[5] M. Krauss and F. Wilczek, "Bolometric detection of neutrinos," *Phys. Rev. Lett*, vol. 55, no. 1, pp. 25–28, Jul. 1985.

[6] K. Tanakaa, A. Odawara, S. Bandou, A. Nagata, S. Nakayama, K. Chinone, A. Yasaka, Y. Koike, and S. Iijima, "Transition edge sensor system for material analysis using transmission electron microscope," *Phys. C*, vol. 469, no. 15–20, pp. 881–885, Oct. 2009.

[7] M. Ellis, "SCUBA-2 CCD-style imaging for the JCMT," *Exp. Astron.*, vol. 19, no. 1–3, pp. 169–174, Jan. 2005.

[8] E. Shirokoff, B. A. Benson, L. E. Bleem, C. L. Chang, H-M. Cho, A.-T. Crites, M. A. Dobbs, W. L. Holzapfel, T. Lanting, A. T. Lee, M. Lueker, J. Mehl, T. Plagge, H. G. Spieler, and J. D. Vieira, "The south pole telescope SZ-receiver detectors," *IEEE Trans. Appl. Supercond.*, vol. 19, no. 3, pp. 517–519, Jun. 2009.

[9] W. Holland, "SCUBA-2: A 10 000 pixel submillimeter camera for the James Clerk Maxwell telescope," in *Proc. SPIE*, 2006, vol. 6275, p. 62 751E.

[10] J. Chervenak, K. Irwin, E. Grossman, J. Martinis, C. Reintsema, and M. Huber, "Superconducting multiplexer for arrays of transition edge sensors," *Appl. Phys. Lett*, vol. 74, no. 26, pp. 4043–4045, Jun. 1999.

[11] K. D. Irwin, "SQUID multiplexers for transition-edge sensors," *Phys. C*, vol. 368, no. 1–4, pp. 203–210, Mar. 2002.

[12] D. J. Benford, G. M. Voellmer, J. A. Chervenak, K. D. Irwin, S. H. Moseley, R. A. Shafer, G. J. Stacey, J. G. Staguhn, J. Wolf, J. Farhoomand, and C. R. McCreight, "Thousand-element multiplexed superconducting bolometer arrays," in *Proc. Far-IR, Sub-MM, MM Detector Workshop*, 2003, pp. 272–275.

[13] J. A. Burney, "Transition-edge sensor imaging arrays for astrophysics applications," Ph.D. dissertation, Stanford Univ., Stanford, CA, 2007.

[14] A. J. Miller, "Development of a broadband optical spectrophotometer using superconducting transition-edge sensors," Ph.D. dissertation, Stanford Univ., Stanford, CA, 2001.

[15] M. Ukibe, M. Koyanagi, M. Ohkubo, H. Pressler, and N. Kobayashi, "Characteristics of Ti films for transition edge sensor microcalorimeters," *Nucl. Instrum. Methods Phys. Res. A, Accel. Spectrom. Detect. Assoc. Equip.*, vol. 436, no. 1/2, pp. 256–261, Oct. 1999.

[16] E. Taralli, C. Portesi, R. Rocci, M. Rajteri, and E. Monticone, "Investigation of Ti/Pd bilayer for single photon detection," *IEEE Trans. Appl. Supercond.*, vol. 19, no. 3, pp. 493–495, Jun. 2009.

[17] P. Roth, G. W. Fraser, A. D. Holland, and S. Trowell, "Modelling the electro-thermal response of superconducting transition-edge X-ray sensors," *Nucl. Instrum. Methods Phys. Res. A, Accel. Spectrom. Detect. Assoc. Equip.*, vol. 443, no. 2/3, pp. 351–363, Apr. 2000.

[18] [Online]. Available: http://www.cadence.com/products/cic/Pages/default.aspx

[19] [Online]. Available: http://www.cadence.com/products/orcad/pages/default.aspx

[20] W. J. Skocpol, M. R. Beasley, and M. Tinkham, "Phase-slip centers and nonequilibrium processes in superconducting tin microbridges," *J. Low Temp. Phys*, vol. 16, no. 1/2, pp. 145–167, 1974.

[21] V. L. Berezinskii, "Destruction of long-range order in one-dimensional and two-dimensional systems possessing a continuous symmetry group. II. Quantum systems," *Sov. Phys. JETP*, vol. 34, no. 3, pp. 610–616, Mar. 1972.

[22] J. M. Kosterlitz and D. J. Thouless, "Ordering, metastability and phase transitions in two-dimensional systems," *J. Phys. C, Solid State Phys.*, vol. 6, no. 7, pp. 1181–1203, 1973.

[23] G. W. Fraser, "On the nature of the superconducting-to-normal transition in transition edge sensors," *Nucl. Instrum. Methods Phys. Res. A, Accel. Spectrom. Detect. Assoc. Equip.*, vol. 523, no. 1/2, pp. 234–245, May 2004.

[24] J. E. Sadleir, S. J. Smith, S. R. Bandler, J. A. Chervenak, and J. R. Clem, "Longitudinal proximity effects in superconductor transition-edge sensors," *Phys. Rev. Lett.*, vol. 104, no. 4, p. 047003, Jan. 2010.

[25] K. D. Irwin, G. C. Hilton, D. A. Wollman, and J. M. Martinis, "Thermal-response time of superconducting transition-edge microcalorimeters," *J. Appl. Phys*, vol. 83, no. 8, pp. 3978–3985, Apr. 1998.

[26] D. A. Bennett, D. S. Swetz, R. D. Horansky, D. R. Schmidt, and J. N. Ullom, "A two-fluid model for the transition shape in transition-edge sensors," *J. Low Temp. Phys.*, vol. 167, pp. 102–107, 2012.

[27] [Online]. Available: http://bwrc.eecs.berkeley.edu/classes/icbook/spice/UserGuide/elements_fr.html

[28] R. M. Kielkowski, *SPICE: Practical Device Modeling*. New York: McGraw-Hill, 1995.

[29] C. J. Fourie and W. J. Perold, "Comparison of genetic algorithms to other optimization techniques for raising circuit yield in superconducting digital circuits," *IEEE Trans. Appl. Supercond.*, vol. 13, no. 2, pp. 511–514, Jun. 2003.

[30] Q. P. Herr and M. J. Feldman, "Multiparameter optimization of RSFQ circuits using the method of inscribed hyperspheres," *IEEE Trans. Appl. Supercond.*, vol. 5, no. 2, pp. 3337–3340, Jun. 1995.

[31] A. Bozbey, S. Miyajima, H. Akaike, and A. Fujimaki, "Single-flux-quantum circuit based readout system for detector arrays by using time to digital conversion," *IEEE Trans. Appl. Supercond.*, vol. 19, no. 3, pp. 509–513, Jun. 2009.

[32] [Online]. Available: http://www.wrcad.com/wrspice.html

[33] R. S. Nebosis, A. D. Semenov, Y. P. Gousev, and K. F. Renk, "Rigorous analysis of a superconducting hot-electron bolometer mixer: Theory and comparison with experiment," in *Proc. 4th Int. Symp. Space Terahertz Tech.*, 1996, pp. 601–613.

[34] H. Merkel, "A hot spot model for HEB mixers including Andreev reflections," in *Proc. 16th Int. Symp. Space Terahertz Tech.*, 2006, pp. 404–415.

Tian-Shun Wang was born in Henan Province, China, on November 7, 1986. He received the B.S. degree in optical information science and technology from Southwest University of Science and Technology, Mianyang, China, in 2009. He is currently working toward the Ph.D. degree at the University of Science and Technology of China, Hefei, China, working on superconducting transition-edge sensor technology.

Guang-Can Guo, biography not available at the time of publication.

Qing-Feng Zhu received the B.S. and M.S. degrees from the University of Science and Technology of China, Hefei, China, in 1996 and 1999, respectively, and the Ph.D. degree from The University of Texas at Austin, Austin, in 2006.

He had worked in Rochester Institute of Technology. He is currently an Associate Professor with the Department of Astronomy, University of Science and Technology of China. His research interests include astronomical instrumentation and infrared/radio astronomy.

Jun-Xian Wang, biography not available at the time of publication.

Tie-Fu Li received the B.S. and Ph.D. degrees from Tsinghua University, Beijing, China, in 2003 and 2009, respectively.

He is currently an Assistant Professor with the Institute of Microelectronics, Tsinghua University. His research interests include quantum computation and nanoelectronics.

Jian-She Liu, biography not available at the time of publication.

Wei Chen received the Bachelor's degree from Zhejiang University, Hangzhou, China, in 1982, the Master's degree from the Chinese Academy of Sciences, Beijing, China, in 1986, and the Ph.D. degree in microelectronics from the University of Cambridge, Cambridge, U.K., in 1995.

He is currently a Professor with the Institute of Microelectronics, Tsinghua University, Beijing. His research interests include the realization of quantum information process using superconducting devices.

Xingxiang Zhou received the Ph.D. degree in electrical engineering from the University of Rochester, Rochester, NY, in 2004.

He is currently with the Department of Optics and Optical Engineering, University of Science and Technology of China, Hefei, China. His research interests include superconducting electronics and quantum computation.